
High-Precision Measurements of the Equation of State of Hydrocarbons at 1 to 10 Mbar Using Laser-Driven Shock Waves

Introduction

Shock waves are routinely used to study the behavior of materials at high pressure. Recently, laser-driven shock waves provided equation-of-state (EOS) data for a variety of materials used in high-energy-density ($E/V \geq 10^{11}$ J/m³) physics experiments at pressures above 1 Mbar (Refs. 1–3). Such data are relevant to inertial confinement fusion (ICF) targets for the National Ignition Facility (NIF), where multiple shock waves are used to provide an approximate isentropic compression of the fusion fuel.^{4,5} Understanding how polymer ablators respond to several-Mbar shock waves is critical to optimizing target performance.

Some of the NIF indirect-drive ablators will be made of glow-discharge polymer (GDP) (C₄₃H₅₆O) with various levels of germanium doping (Ge-GDP).^{6,7} No high-pressure data exist for these materials. Polystyrene (CH) is closest in structure and was considered a coarse indicator for shock-timing simulations of NIF targets involving such ablators. Shocked polystyrene has been studied using gas-gun drivers up to ~0.5 Mbar and laser-driven shock waves between ~7 to 41 Mbar (Refs. 8–10). Experiments above 1 Mbar (Refs. 8 and 9) had large error bars and appeared to behave noticeably stiffer than the models used to match the low-pressure data. Moreover, there was no verification of material behavior in the pressure range relevant to the NIF multiple-shock compression scheme, where successive shocks produce pressures of around 1 to 10 Mbar.¹¹ The use of these limited, low-precision data for polystyrene to predict the behavior of NIF Ge-doped ablator materials provides an unacceptable uncertainty.

Ultimately, the goal is to verify and understand the behavior of Ge-GDP at pressures of 1 to 10 Mbar. EOS models for this material will likely be based on existing models for polymers. To this end, we first address the behavior of polystyrene to determine whether this material indeed behaves stiffer than predicted, as suggested by Refs. 8 and 9. Next, the effect of stoichiometry (C-to-H ratio) is studied by measuring the EOS of polypropylene. Having quality EOS data on these two materials will provide a basis on which models of more-complicated

polymers (Ge-GDP) can be based. This article reports the results of precise EOS measurements on polystyrene and polypropylene and compares them to existing data.

Polystyrene and polypropylene (CH₂) are relatively simple organic compounds, composed solely of hydrogen and carbon. Atoms in each polymer molecule are covalently bonded, while attraction between molecules can include Van der Waals forces, dipole interactions, and hydrogen bonds.¹² These hydrocarbons are thought to experience chemical decomposition into phases of diamond-like C and H (Ref. 13) at sufficiently high pressures and temperatures. Several studies have demonstrated this using principal Hugoniot data in the 0.01- to 1-Mbar regime.^{13,14} Electrical conductivity measurements¹⁵ in a similar pressure range showed a predictable dependency on the C-to-H ratio in the hydrocarbons. Studying CH and CH₂ in the high-energy-density regime opens the possibility of observing high-pressure chemistry.

In the present study, laser-driven shock waves were used to produce high-precision impedance-matching (IM) measurements using quartz as a reference material.^{1,16–18} This provided ~1% precision in shock-velocity measurements. Single-shock measurements were performed on CH and CH₂, showing that both materials undergo similar compressions between 1 to 10 Mbar, although their behavior in the P - ρ plane is distinctly different. Measurements of reflectance and brightness temperatures show that these two hydrocarbons behave similarly at high pressures. Additionally, polystyrene's behavior under double-shock compression was measured, and those results were consistent with single-shock results. All measurements are compared with available models and previous works.

In the following sections, experimental conditions including diagnostics and targets are described; the IM technique, including single- and double-shock states, is discussed, with emphasis on improvements that enable one to acquire high-precision data; high-precision velocity measurements and error analysis are discussed in more detail; and, finally, results are presented, followed by concluding remarks.

Experiment

Experiments were performed on LLE's OMEGA Laser System.¹⁹ Shock pressures of 1 to 10 Mbar were produced by laser energies between 200 J and 1130 J delivered in 2-ns temporally square pulses of 351-nm light. The laser's focal spot was smoothed using distributed phase plates,²⁰ resulting in nearly uniform irradiation spots with diameters of either 600 or 800 μm . The average laser intensity was between 0.3 and 1.1×10^{14} W/cm².

The targets for the single-shock measurements consisted of 90- μm pushers made of z -cut α -quartz with the samples mounted on the rear side. The samples were 50- μm -thick CH and/or CH₂ foils. Impedance measurements were performed at the interface between the quartz and the sample.^{21,22} A second set of targets for CH EOS consisted of "anvil" targets, having a second piece of z -cut α -quartz glued onto the back of the 50- μm CH sample. For these targets, single-shock measurements were obtained at the first interface (quartz-to-sample), and re-shock measurements were obtained at the second interface (sample-to-quartz), where the shock in the sample reflected off the denser quartz. The glue layers were kept below a few microns. The use of 90- μm -thick pushers minimized preheating of the sample. The laser-produced plasmas that drove these shock waves had temperatures of 1 to 2 keV. The soft- and mid-energy x rays from such plasmas were absorbed in the first half (laser side) of the quartz pusher.

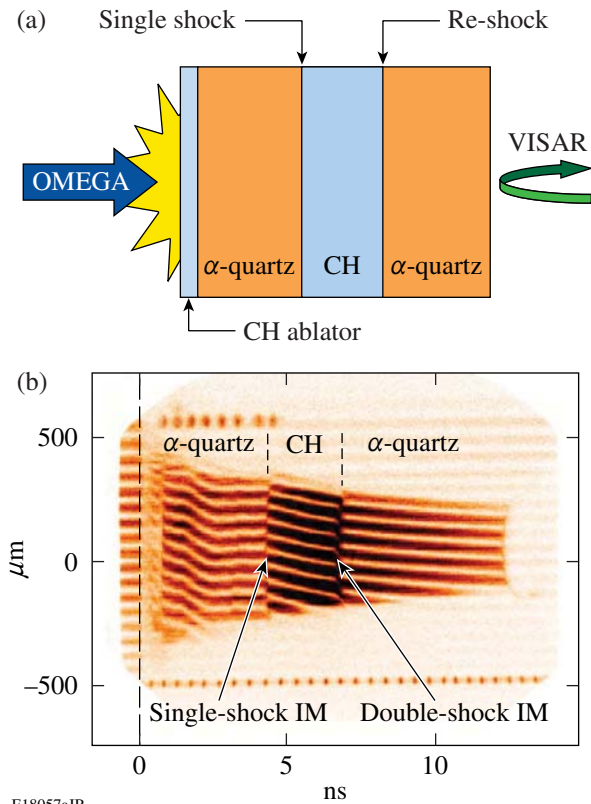
All targets had a 20- μm CH ablator (on the laser side) to absorb the incident laser and reduce the production of x rays that might preheat the samples. To minimize ghost reflections, the free surface of the samples and the quartz anvils had antireflection coatings. Material densities were 2.65 g/cm³ for quartz, 1.05 g/cm³ for CH, and 0.90 g/cm³ for CH₂. The index of refraction for these materials at the 532-nm probe-laser wavelength was 1.55, 1.59, and 1.49 for quartz, CH, and CH₂, respectively.

A line-imaging velocity interferometer system for any reflector (VISAR)^{23–26} measured shock velocities in the samples. The drive pressures were sufficient to produce optically reflective shock fronts in both the quartz and the polymer samples (see **Optical and Thermal Measurements**, p. 16). This resulted in direct, time-resolved measurements of the shock velocity in both the pusher and the samples. Two VISAR's with different velocity sensitivities were used to discern the 2π phase-shift ambiguity that occurs when the shock velocity instantaneously jumps at material interfaces. Etalons of 18-mm and 7-mm thickness were used to produce uncorrected velocity

sensitivities of 2.732 and 6.906 $\mu\text{m}/\text{ns}/\text{fringe}$, respectively. The indices of refraction determined the VISAR sensitivity in each material. The VISAR data were analyzed with a fast Fourier transform (FFT) method that determines fringe position to $\sim 5\%$ of a fringe. Since the shock speeds used in these experiments typically cause approximately five fringe shifts, velocities are measured to $\sim 1\%$ precision (lower shock speeds produce slightly larger velocity errors). Shock-front reflectivity information is encoded in the fringe pattern and can be obtained by measuring its amplitude after applying the FFT. Since the drive pressures are high enough to cause metallic-like states in the materials, the probe-laser reflection occurs within the skin depth (~ 100 nm or less)²³ of the metalized fluid; this, along with the steep shock front, produces a highly reflective surface. The probe laser for VISAR was a Q -switched, injection-seeded Nd:YAG laser operating at 532 nm with a pulse length of ~ 50 ns at full width at half maximum (FWHM). The reflected probe signal was detected by a ROSS²⁷ streak camera, one for each VISAR, having either 15- or 9-ns temporal windows. The response time of the diagnostic was dominated by the delay time associated with the etalons—90 or 40 ps.

An absolutely calibrated streaked optical pyrometer (SOP)²⁸ was used simultaneously with VISAR. The SOP measured the visible and near-infrared self-emission from the shock front as it propagated through the target. Its wavelength-dependent spectral responsivity was determined by the relay optics, diagnostic filtration (long pass filter with a cutoff wavelength of 590 nm), and streak camera photocathode response, defining a red channel from 590 to 900 nm. The device was absolutely calibrated using a NIST-traceable tungsten lamp and power supply.²⁸ The temporal window of the diagnostic was set to 10 or 20 ns, depending on expected irradiances on target. Using a 500- μm slit and a 10-ns temporal window led to an ~ 170 -ps temporal response time.²⁸ The SOP provides a temporal history of shock-front temperature. The VISAR and SOP are temporally calibrated so that combining the data provides temperature as a function of velocity and, consequently, temperature as a function of pressure.

The experimental configuration is shown in Fig. 121.4(a). The OMEGA Laser System irradiates the CH ablator on the front of the EOS targets, producing a shock wave that traverses the quartz pusher, sample, and quartz anvil (the quartz anvil was not used for all experiments). The VISAR and SOP view the rear side of the target, and since each of these layers is transparent, they measure the shock velocity and self-emission inside each layer. Figure 121.4(b) shows VISAR data for an anvil target. The horizontal lines are the VISAR fringes whose vertical



E18057aJR

Figure 121.4

(a) Schematic of planar anvil targets used in the experiments. The laser drive irradiates the target from the left, while the VISAR probe beam reflects off the shock from the rear side of the target (right). (b) VISAR streak image, showing continuous track of shock front within standard and sample.

position is proportional to the shock velocity. Before $t = 0$, the fringes are horizontal and constant because no shock wave is present. The x rays from the laser-driven plasma (which start at $t = 0$) caused the CH ablator to become opaque. As a result, the VISAR fringes disappear from $t = 0$ to ~ 0.7 ns. At 0.7 ns the shock wave enters the quartz, where the VISAR detects it. The shock-wave strength decays as it transits the quartz but soon stabilizes as the rarefactions equilibrate the pressure between the target layers and the ablation front driven by the laser. This produces a relatively steady shock from 2 to 4.3 ns.

At 4.3 ns, the shock wave transits the quartz–CH interface and enters the CH, where its velocity changes. This is seen as a jump in the position of the VISAR fringes and an abrupt change in their intensity. The latter is a result of the difference in the reflectivities of the shock waves in quartz and CH. The single-shock IM measurement is made across this interface. At 6.7 ns the shock wave reaches the quartz anvil and the fringe position and intensity change again. The double-shock (re-shock) IM measurements are made at this interface.

Note in Fig. 121.4(b) that the observed quartz–CH interface has a finite temporal width; this is the region where the shock transits the thin glue layer. In addition, the VISAR response time (given by the etalon thickness) is 40 ps and 90 ps. The shock velocities are, therefore, not measured directly at the contact interface between materials. This is accounted for by linearly fitting the shock velocities at least 0.3 ns before and after the interface transition region and extrapolating to the “ideal” interface. This also accounts for any slope present in these velocity profiles.

Compared to previous studies on hydrocarbons in the Mbar range, this study is novel in both the precision (1%) of the velocity measurements and the treatment of the errors in the IM technique: both random and systematic errors are evaluated. The next section describes the IM technique and the error analysis used for this study.

Impedance-Matching Analysis

1. Single-Shock Experiments

The jump conditions for shock waves are described by the Rankine–Hugoniot relations derived from the conservation of mass, momentum, and energy; they relate pre- and post-shock conditions via particle velocity (U_p) and shock velocity (U_s),^{21,22} as

$$P_1 - P_0 = \rho_0 U_s U_p, \quad (1)$$

$$\rho_1 (U_s - U_p) = \rho_0 U_s, \quad (2)$$

$$E_1 - E_0 = \frac{1}{2} (P_1 + P_0) \left(\frac{1}{\rho_0} - \frac{1}{\rho_1} \right), \quad (3)$$

where subscripts 0 and 1 denote initial and shock conditions in terms of pressure P , density ρ , and internal energy E . The first two equations have four unknowns (given that the initial pressure and density are known) and can be solved by measuring two variables. This solution constitutes a kinematic equation of state and is often defined as U_s as a function of U_p . High-pressure shock waves are typically reflecting, allowing one to optically measure the shock velocity, but usually preventing direct optical measurement of the particle velocity. The IM technique is used to infer the particle velocity by referencing the sample under study to a standard material whose equation of state is known.^{21,22}

The conservation equations dictate that the pressure and particle velocity are conserved across the contact interface between the standard and the sample. This makes it possible to infer the common particle velocity from the shock velocities in the standard and the sample, as the shock wave enters and exits the contact interface between the materials. This is shown in Fig. 121.5(a) in the pressure–particle velocity ($P-U_p$) plane. A measurement of the shock velocity in the standard provides the initial condition of the shock wave before it interacts with the sample. This state (A) is the intersection of the Rayleigh line ($P = \rho_0 U_s U_p$) and the known Hugoniot for the standard. If the sample has lower impedance than the standard, the standard will undergo isentropic release until its impedance “matches” that of the sample, when the continuity equations are satisfied across the interface between the standard and the sample. This determines the shocked state of the sample [state (B) in Fig. 121.5(a)]. This shocked state is the intersection between the release curve for the standard and the Rayleigh line defined by the measurement of the shock velocity in the sample. By measuring two shock velocities (one in the standard and one in the sample), the particle velocity in the sample can be inferred. The U_s and U_p for the sample define the equation of state of the sample. Care must be taken to ensure that the measured shock velocities are those just before and just after the shock wave crosses the interface between the two materials. The shock-wave jump conditions are a consequence of conservation of mass and momentum, which are always satisfied regardless of shock stability. Therefore, shock steadiness is not a requirement for IM with transparent standards since jump conditions for a shock hold for decaying (and increasing) shock waves. If the measurement has sufficient time resolution, the requirement for shock steadiness can be relaxed as long as the variation in velocity can be measured.

The IM technique requires knowledge of the Hugoniot and release behavior of the standard. The precision of the data obtained through the IM technique depends on the accuracy with which the states in the standard are known. The quartz principal Hugoniot was studied in the high-pressure fluid regime (2 to 15 Mbar) using laser-driven shock waves.¹ That study bridged the gap in data between existing gas-gun,^{29,30} explosively driven,³¹ and nuclear-driven³² experiments. The laser-driven data were consistent with previous studies having longer characteristic time scales. This indicates that the shock waves equilibrate on time scales shorter than the measurement times in laser experiments. The data show that shocked quartz is solid up to about 1 Mbar; above 1 Mbar shocked quartz melts and becomes reflective. The EOS of quartz is characterized by a piecewise linear U_s-U_p relationship of the general form $U_s = a_0 + a_1(U_p - \beta)$ as

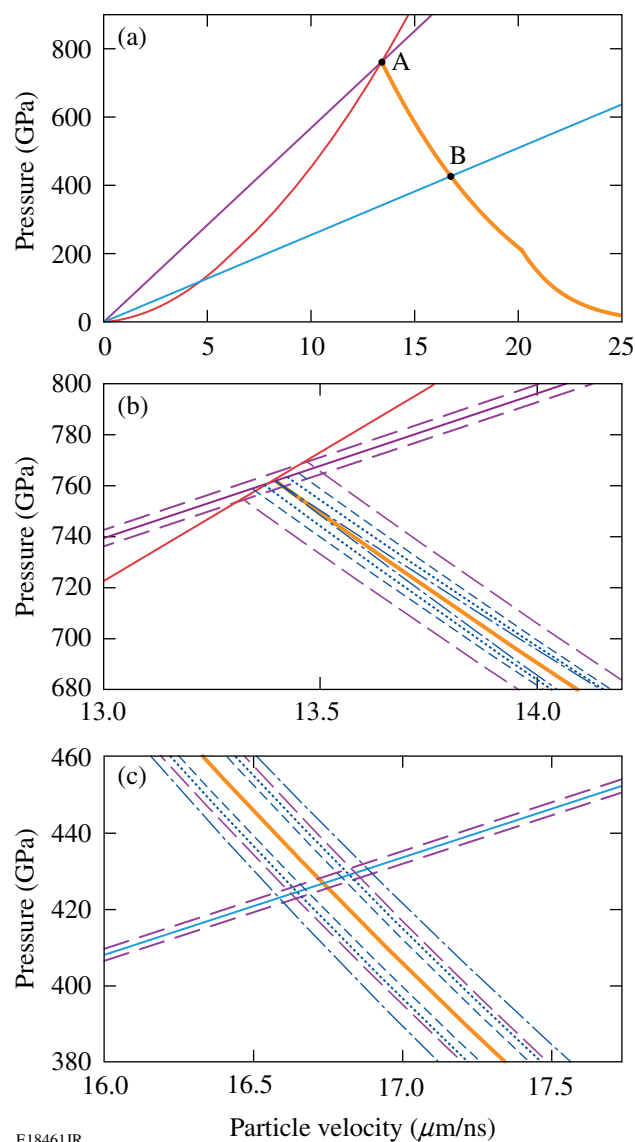


Figure 121.5 Sample IM construct with inclusion of errors for a 7.6-Mbar shock propagating from quartz to CH. Total errors are found by taking the quadrature sum of random and systematic uncertainties. (a) General IM diagram. Rayleigh lines for quartz and CH are shown as purple and light blue lines, respectively, while red and orange solid curves correspond to the principal Hugoniot and release of quartz. (b) Errors associated with quartz’s initial shock state and release variation from nominal. Systematic contributions are shown in dark blue and random contributions are shown in purple. Error in quartz’s Rayleigh line is shown by purple dashed lines. This causes a random variation propagated as an offset release curve, shown as purple dashed lines. Systematic variations from nominal release are shown as dark blue dashed–dotted, dashed, and small dashed curves, corresponding to $\delta\Gamma$, δa_0 , and δa_1 , respectively. (c) Final variations from a nominal (U_p, P) state are depicted by intersections between the nominal CH Rayleigh line and previously mentioned releases caused by random and systematic error contributions. A second random error contribution is found through the intersection between nominal quartz release and the CH Rayleigh line with $\delta U_{s,CH}$ contribution, shown as a purple dashed line.

$$U_s = (6.914 \pm 0.028) + (1.667 \pm 0.038)(U_p - 3.0244), \quad (4)$$

for $U_p < 6.358 \mu\text{m/ns}$,

$$U_s = (19.501 \pm 0.068) + (1.276 \pm 0.022)(U_p - 11.865), \quad (5)$$

for $U_p \geq 6.358 \mu\text{m/ns}$,

where an orthonormal basis is used so that the resulting errors are uncorrelated.¹⁸ This U_s - U_p relation was used in this work.³³ The quartz was shocked to 1 to 15 Mbar, producing reflective shock waves that allowed for VISAR measurements of the shock velocity, thereby providing the initial state of the standard for IM.

The quartz's impedance was matched to the sample when its release isentrope intersected the Rayleigh line in the sample. Quartz's release isentropes were calculated using the Mie-Grüneisen formalism as described in previous works.^{18,34} In this work's analysis, the reflected experimental Hugoniot was used, resulting in isentropes that follow a piecewise behavior stemming from the description of quartz's principal Hugoniot EOS, as described by Eqs. (4) and (5) [Fig. 121.5(a)]. For strongly shocked quartz in the dense fluid regime, calculations of the Mie-Grüneisen parameter based on solid and porous silica Hugoniot measurements^{1,32,35} showed Γ to be nearly constant with a value $\Gamma = 0.66 \pm 0.1$ (Ref. 18). Inspection of various EOS models for silica in the high-pressure fluid regime led to a constant value $\Gamma = 0.64 \pm 0.11$ (Ref. 2), consistent with the experimentally derived value. This latter model-based value for Γ and its associated error were used in this work. The value of Γ is the only model-dependent parameter used here.

The total error in the measured U_p , P , and ρ is the quadrature sum of the random and systematic errors inherent in the IM technique. Random errors originate in the shock-velocity measurements in both the quartz and samples. Systematic uncertainties arise from errors in the EOS of the standard, i.e., the a_0 and a_1 coefficient of quartz's experimentally derived principal Hugoniot, and from the Mie-Grüneisen parameter Γ . The relative contributions of these errors varied over the range of pressures studied.

2. Double-Shock Experiments

The above discussion of the IM technique applies to single-shock measurements, i.e., the standard and sample both experience a single shock wave. Multiple shock waves

produce off-Hugoniot states that are pertinent to ICF target designs that employ multiple shock waves to approximate isentropic compression. Double-shock measurements can validate models since they amplify small differences in the principal Hugoniot.³⁶

A double-shock measurement was created in these experiments by placing a second slab of quartz behind the samples, creating an "anvil" target. The shock wave traveled through the first layer of quartz into the polymer (where single-shock Hugoniot data were obtained). When the shock wave in the sample reached the second layer of quartz, it was reflected back into the sample. The conservation equations applied at this sample-quartz interface and a second IM measurement provided the U_p and P for the double-shocked sample. The important measurements were the shock velocity in the sample just before it impacted the quartz and the velocity of the shock wave just after it entered the quartz. The former provided the initial single-shock state of the CH, and the quartz's shock velocity provided the pressure of the second shock wave (which was conserved between the sample and the quartz).

High-Precision Velocity Measurements

Since quartz is transparent, its use as a standard^{1,16-18} provides high-precision EOS data because instantaneous velocities can be measured before and after the IM point (provided the sample is transparent). Several other studies have demonstrated precise IM measurements using quartz as a standard.^{2,37}

The continuity equations are central to the IM technique. As the shock traverses the interface, the materials accelerate, expand, and experience shock, reshock, or release, to equilibrate and satisfy those conditions. The use of a quartz standard and VISAR with high temporal resolution significantly reduces the inaccuracies by providing "instantaneous" measurements. In this study, shock velocities were measured to ~1% precision. Trends in the temporal profile of the observed velocities were linearized over the ~300 ps before and after the quartz-sample interface and extrapolated to that interface. This accounted for both the unsteadiness of the shock and the response time of VISAR (i.e., the etalon delays).

The usefulness of EOS data is determined by the size and validity of the error bars. As the precision of the velocity measurements increases, the effects of systematic errors become increasingly important. The random and systematic errors are rigorously accounted for in this study, and the total uncertainties are found by calculating the quadrature sum of random and systematic errors.

The total uncertainties for U_p , P , and ρ , each obtained through the IM technique, depend on seven error contributions: δU_{sQ} , δU_{sCH_x} , δa_{0L} , δa_{0H} , δa_{1L} , δa_{1H} , and $\delta \Gamma$. The first two are random errors, associated with the two shock-velocity measurements. The last five are systematic errors, of which the first four are fitting parameters for the quartz experimental Hugoniot $U_s = a_0 + a_1(U_p - \beta)$, where subscripts L and H correspond to fitting parameters to the low ($U_p < 6.358 \mu\text{m/ns}$) and high ($U_p \geq 6.358 \mu\text{m/ns}$) linear fits. The last ($\delta \Gamma$) is used to approximate quartz's release isentrope by assuming a Mie–Grüneisen EOS and having knowledge of quartz's principal Hugoniot.

Figures 121.5(a)–121.5(c) show a graphical description of the IM analysis and the errors encountered. Measurement errors δU_{sQ} produce a random uncertainty in the quartz's initial shocked state, producing multiple possible Rayleigh lines that can intersect the quartz Hugoniot at different points. Systematic errors in the quartz Hugoniot produce uncertainty in this initial state. These are shown as the 1σ variation in quartz Hugoniot. Continuing with this formalism, each of these possible states can be the initial condition for the isentropic release of quartz, which has errors associated with a_0 , a_1 , and Γ . These release curves form a cascade of possible release curves that the standard could follow. Figures 121.5(b) and 121.5(c) indicate the quantitative bounds on the release curves that can be used for an IM solution.

The state of the shocked sample and therefore the final state of the quartz release were determined by the measured shock velocity in the sample. Errors in this measurement, δU_{sCH_x} , produced multiple Rayleigh lines that intersect with the various release curves. Rigorous propagation of these errors provides confidence in the error bars that were assigned to the pressure and particle velocity inferred from the IM technique.

The total uncertainty for the derived IM variables is found by taking the quadrature sum of the error contributions. The predominance of random or systematic uncertainties varies with pressure. At low pressures (lower velocities), random uncertainties dominate because the phase excursion results in fewer fringes and the 5% error in fringe location is more significant. Shock-front reflectivities are lower, resulting in lower VISAR signal levels. At higher pressures, the random uncertainties become smaller. At pressures of ~ 9 Mbar in CH, corresponding to quartz pressures of ~ 15 Mbar, systematic uncertainties are around $3\times$ larger than random uncertainties. This results from the lower accuracy of the quartz Hugoniot at these higher pressures, making it increasingly difficult to perform precision measurements.

Kinematic Results

1. Polystyrene (CH)

The single-shock results for polystyrene (see Table 121.I) are shown as orange squares in Fig. 121.6, a U_s-U_p plot that also contains previous results and various models.³⁸ This study's data were fit with the line $U_s = (21.029 \pm 0.057) + (1.305 \pm 0.015)(U_p - 14.038)$, derived using a least-squares fit of the data set with their total error over an orthogonal polynomial basis; this produced uncorrelated errors in the coefficients of the fit. The total error bars for this study are smaller than the random-only errors of other works. The benefit of these smaller errors is demonstrated in Fig. 121.7 showing the various data and models in the $P-\rho$ plane. The error derived in density scales as $(\eta-1)$ times the errors in shock velocity, where η is the compression (ρ/ρ_0) (Ref. 39). Here the difference in results and models is more apparent.

The data are compared to three *SESAME* models (refer to Figs. 121.6 and 121.7). *SESAME* 7591 and 7592 are similar in the method used to calculate the electronic, nuclear, and 0 K isotherm contributions to the total EOS, where differences arise from certain input parameters used to carry out these calculations. The electronic contribution for both models is calculated via a temperature-dependent Thomas–Fermi–Dirac (TFD) model, with assumption of an average atom, where the exchange parameter is equal to $2/3$. The cold curve is obtained from principal Hugoniot measurements and the assumption of a Mie–Grüneisen EOS. At low densities the solution is matched to the Lennard–Jones formula, and at high densities it is matched to calculations obtained through TFD. In addition to the atomic weight (6.510), atomic number (3.5), and initial density, a reference Grüneisen parameter and Debye temperature are required for the cold curve construct. The reference Grüneisen parameter is calculated from experimental values of the specific heat at constant pressure, the isentropic bulk modulus, the thermal expansion coefficient, and the initial density. *SESAME* 7591 adjusts the value of the reference Grüneisen parameter from 0.565 (value used for *SESAME* 7592) to 0.5 in order to reproduce shock EOS data for porous polystyrene. *SESAME* 7591 has higher values for the reference Debye temperature and temperature of melt by $\sim 16\%$ compared to *SESAME* 7592. The available low-pressure shock data are better predicted by *SESAME* 7592, which closely follows the change in slope in the U_s-U_p plane between 2 to 4 $\mu\text{m/ns}$ in U_p . Cohesive energies used in the cold curve calculations are also different between these models: *SESAME* 7591 uses a higher cohesive energy calculated from the heat of vaporization of carbon and the dissociation energy of hydrogen, while for *SESAME* 7592 the cohesive energy was set at

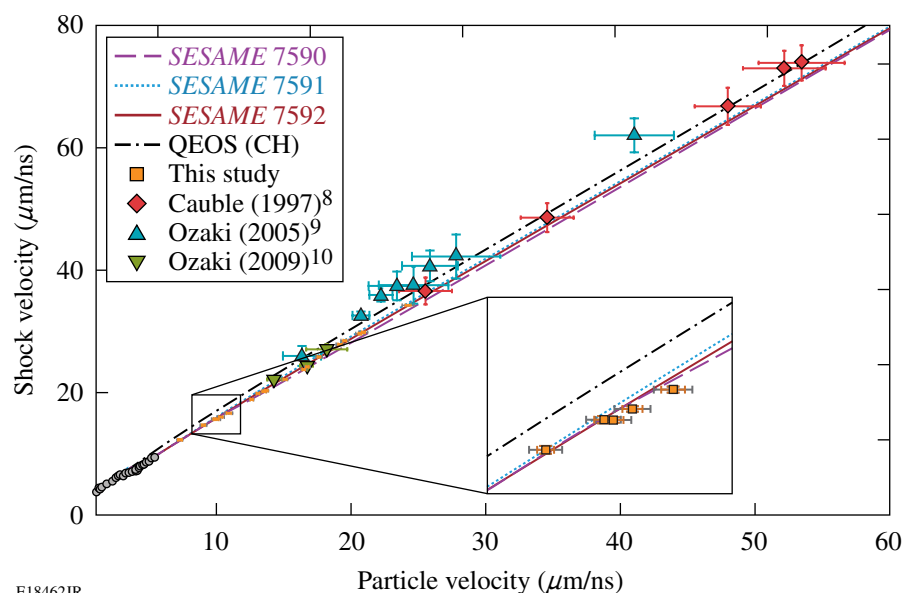


Figure 121.6

Principal Hugoniot data and models for CH in the U_s-U_p plane. Data for this study were taken on polystyrene (C_8H_8)_n, with initial density $\rho_0 = 1.05$ g/cc, using IM with quartz reference. Random uncertainties are shown as orange error bars and total uncertainty (quadrature sum of random and systematic errors) are shown as gray error bars. Previous gas-gun experiments (gray circles);^{30,40-43} absolute measurements on NOVA (red diamonds);⁸ and IM experiments on GEKKO using aluminum⁹ and quartz¹⁰ reference (cyan and green triangles, respectively). Various SESAME³⁸ models are shown along with a QEOS model.

E18462JR

Table 121.I: Polystyrene principal Hugoniot results from impedance matching with quartz reference. Measured shock velocity in the quartz and polystyrene, U_{sQ} and U_{sCH} , is given with associated random error, arising from measurement limitations. U_{pCH} (ran,sys), P_{CH} (ran,sys), and ρ_{CH} (ran,sys) are the resulting particle velocity, pressure, and density of shocked polystyrene obtained through the IM construct. Random errors enter the analysis through measurement uncertainties in U_{sQ} and U_{sCH} , while systematic errors emerge from uncertainties in the principal Hugoniot and release states of quartz.

Shot No.	U_{sQ} ($\mu\text{m/ns}$)	U_{sCH} ($\mu\text{m/ns}$)	U_{pCH} (ran,sys) ($\mu\text{m/ns}$)	P_{CH} (ran,sys) (Mbar)	ρ_{CH} (ran,sys) (g/cc)
52795	11.73±0.19	12.36±0.11	7.26 (0.16, 0.13)	0.94 (0.02, 0.02)	2.54 (0.09, 0.06)
52800	13.68±0.1	14.76±0.12	9.01 (0.12, 0.21)	1.4 (0.02, 0.03)	2.7 (0.07, 0.1)
52793	14.47±0.11	15.74±0.12	9.86 (0.14, 0.22)	1.63 (0.02, 0.04)	2.81 (0.08, 0.1)
52124	14.59±0.12	15.73±0.09	10.01 (0.15, 0.22)	1.65 (0.03, 0.04)	2.89 (0.08, 0.11)
52464	14.85±0.12	16.09±0.09	10.29 (0.15, 0.22)	1.74 (0.03, 0.04)	2.91 (0.08, 0.11)
52628	15.38±0.14	16.72±0.1	10.89 (0.18, 0.22)	1.91 (0.03, 0.04)	3.01 (0.1, 0.11)
52792	17.09±0.09	18.95±0.12	12.6 (0.1, 0.1)	2.51 (0.02, 0.02)	3.13 (0.07, 0.05)
52463	17.63±0.1	19.92±0.1	13.06 (0.11, 0.1)	2.73 (0.03, 0.02)	3.05 (0.06, 0.05)
52631	18.08±0.12	20.27±0.12	13.51 (0.14, 0.11)	2.88 (0.03, 0.02)	3.15 (0.08, 0.05)
52799	18.23±0.12	20.41±0.12	13.66 (0.14, 0.11)	2.93 (0.03, 0.02)	3.18 (0.08, 0.05)
52791	19.72±0.12	22.26±0.1	15.08 (0.14, 0.14)	3.52 (0.03, 0.03)	3.25 (0.07, 0.06)
52634	21.16±0.1	23.87±0.13	16.46 (0.11, 0.17)	4.13 (0.03, 0.04)	3.38 (0.07, 0.08)
52122	21.46±0.09	24.3±0.09	16.73 (0.11, 0.17)	4.27 (0.03, 0.04)	3.37 (0.06, 0.08)
52118	22.45±0.1	25.92±0.12	17.6 (0.12, 0.19)	4.79 (0.04, 0.05)	3.27 (0.06, 0.08)
52121	24.1±0.13	27.98±0.1	19.16 (0.15, 0.23)	5.63 (0.05, 0.07)	3.33 (0.07, 0.09)
52117	24.49±0.11	28.58±0.1	19.51 (0.12, 0.24)	5.86 (0.04, 0.07)	3.31 (0.05, 0.09)
52113	25.64±0.11	29.73±0.16	20.64 (0.13, 0.27)	6.44 (0.05, 0.08)	3.43 (0.07, 0.1)
52633	25.89±0.12	29.94±0.14	20.89 (0.14, 0.27)	6.57 (0.05, 0.09)	3.47 (0.07, 0.11)
52119	29.42±0.18	34.36±0.11	24.22 (0.21, 0.37)	8.74 (0.08, 0.13)	3.56 (0.08, 0.13)

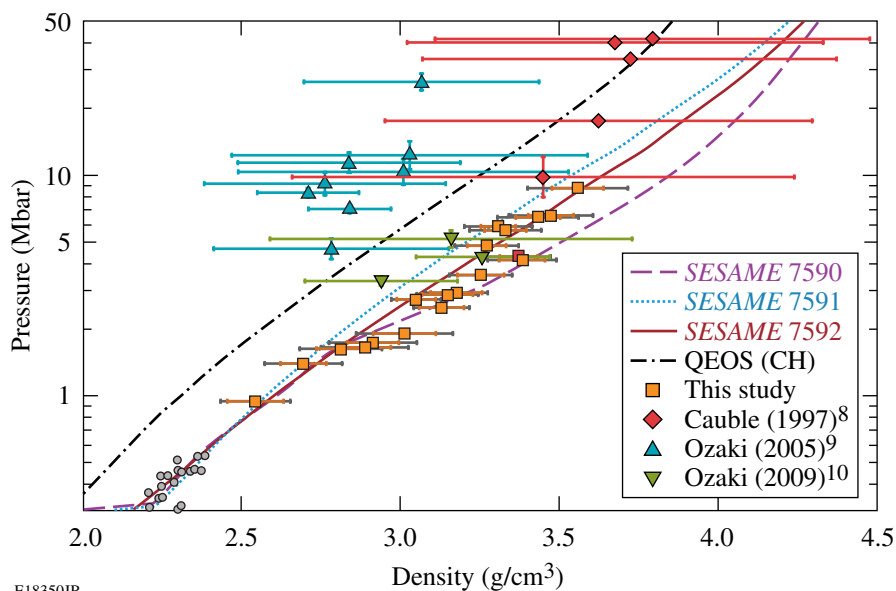


Figure 121.7

Principal Hugoniot data and models for CH in the P - ρ plane. Data for this study were taken on polystyrene (C_8H_8)_n, with initial density $\rho_0 = 1.05$ g/cc, using IM with quartz reference. Random uncertainties are shown as orange error bars and total uncertainty (quadrature sum of random and systematic errors) are shown as gray error bars. Previous gas-gun experiments (gray circles);^{30,40–43} absolute measurements on NOVA (red diamonds);⁸ and IM experiments on GEKKO using aluminum⁹ and quartz reference¹⁰ (cyan and green triangles, respectively). Various *SESAME*³⁸ models are shown along with a QEOS model.

15 kcal/mole (~ 4.8 MJ/kg) in order to reproduce the critical point. The nuclear models calculate the kinetic contribution of atoms and ions in both solid and gas. Lattice vibrational contributions are carried out assuming a Debye–Grüneisen solid; therefore, the reference Grüneisen parameter and Debye temperature are also used in these calculations. At high temperatures or low densities, this nuclear term describes an ideal gas, where ideal mixing is used. These limiting theories are joined by means of interpolation functions.^{38,44,45} No detailed information of the construction of *SESAME* 7590 was available.

SESAME 7592 appears to best model the present data for polystyrene, although a slight softening with respect to this model is observed between 2 and 4 Mbar. It is thought that at intermediate pressures, the C–H bonds in these polymers undergo chemical decomposition, favoring C–C and H–H bonds. It is possible that the softening at 2 to 4 Mbar indicates these bonds are breaking. This represents an energy sink that could explain the softening.

Previous results by Cauble *et al.*⁸ (absolute data) and Ozaki *et al.*⁹ (IM with an aluminum standard) show distinctly stiffer behavior than these data and most of the models, as shown in Fig. 121.7. These authors have stated, post publication, that their results likely suffered from x-ray preheating of the samples.⁴⁶ The newest data from Ozaki *et al.*¹⁰ used thicker pushers and low- Z ablaters to reduce preheat of the samples. Those experiments also used IM with a quartz standard and show results (green triangles in Fig. 121.7) that are much closer to this work.

In the anvil targets the shocks that reflect off the rear quartz layer produced double-shocked states in CH; these states were measured using the IM at that reflection point (see Table 121.II). The pressure reached in double-shock experiments is highly dependent on the initial state from which it launches, being particularly sensitive to the single-shock density. Because of this dependence, double-shock measurements provide a valuable tool to assess single-shock densities reached in CH. It is difficult to deconvolve measured quantities and model-dependent effects originating from the use of a standard material in the impedance-matching technique; in this aspect, double-shock measurements provide another advantage, where it is possible to separate models and observables, presenting a

Table 121.II: Double-shock states in polystyrene (CH) were probed by using reflected shock waves from anvil targets. Observables, listed below, were used for direct comparison with model behavior.

Shot No.	U_{sQ} ($\mu\text{m/ns}$)	U_{sCH} ($\mu\text{m/ns}$)
52464	11.45 ± 0.16	12.25 ± 0.09
52792	13.27 ± 0.31	14.60 ± 0.09
52463	14.14 ± 0.11	15.80 ± 0.11
52791	15.51 ± 0.10	17.45 ± 0.10
52122	17.25 ± 0.11	19.77 ± 0.09
52118	18.77 ± 0.11	21.71 ± 0.09
52117	20.96 ± 0.11	24.65 ± 0.13
52113	23.22 ± 0.09	27.66 ± 0.11
52119	26.25 ± 0.10	31.59 ± 0.14

sensitive platform for model comparison. Re-shock results are plotted in Fig. 121.8, showing the experimental observables: U_{sQ} versus incident U_{sCH} . Here the associated measurement error bars are quite small. These are compared with double-shock states as predicted by each model. The curves representing each model were produced by performing the IM analysis with each model (using its principal Hugoniot and re-shock curves) and the experimental quartz Hugoniot. The errors produced in this analysis were about the thickness of the lines and stemmed from the experimental errors associated with the quartz fit. The CH shock velocity (U_{sCH}) represents the single-shocked state of the CH, and, based on conservation equations, the re-shocked state of CH is derived from quartz's shock velocity U_{sQ} . Plotting the data in this manner removes any model dependence from the data. Despite the apparent similarity among the models, the small error bars in the data allow one to discriminate between them. This is shown in the inset in Fig. 121.8, an expanded region of the plot near $26 \mu\text{m/ns}$. In this type of plot, a model that assumes the material to be more compressible (softer) will display a higher quartz shock velocity for a given CH shock velocity. These re-shock data show behavior similar to the single-shock data, where a slight softening is observed at single-shock pressures from ~ 2 to 4 Mbar. For single-shock pressures outside this range, double-shock data are in agreement with *SESAME 7592*. Such behavior

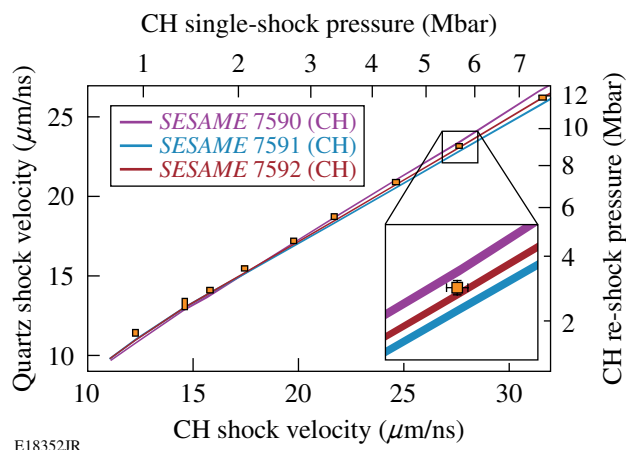


Figure 121.8

Double-shock (re-shock) data for CH using quartz anvil targets. Measured observables are plotted against *SESAME* models,³⁸ displayed as two quasi-parallel lines, resulting from errors associated with quartz experimental EOS fitting parameters. In this plot, softer models will display higher shock velocities in quartz for a given shock velocity in CH. The data are shown as orange rectangles, where the height and width of each are determined by the associated errors in shock-velocity measurements in CH and quartz, respectively. The data are consistent with the *SESAME 7592* model³⁸ at high and low pressures, where there is an evident softening of the data from around 2 to 4 Mbar. This shows agreement between single- and double-shock experiments.

is consistent to that observed in single-shock measurements. The measured quantities for CH re-shock experiments can be found in Table 121.II.

Double-shock results can be directly compared to single-shock data by transforming double-shock observables into single-shock quantities in the P - ρ plane via an inversion method as described by Hicks *et al.* (Ref. 3). This analysis is based on the concept that the double-shock compressibility is better known than the single-shock compressibility—often justified since dissociation along the Hugoniot is the largest source of uncertainty in the models. Such an inversion method uses the Hugoniot equations for the single- and double-shock states and an average of several models (in this case *SESAME* models for polystyrene) to predict the re-shock state through calculation of a model-based averaged adiabatic exponent. By using the double-shock pressure and particle velocity obtained from the measured shock velocity in quartz and quartz's experimental fit, and the shock velocity in the single-shock state, one arrives at a single-shock pressure and density. The results of this analysis (yellow diamonds) are shown in Fig. 121.9, along with the single-shock data. The total uncertainty associated with the inferred single-shock results is represented by black error bars. The total uncertainty is the quadrature sum of systematic uncertainties stemming from the 1σ variation in the averaged model-based adiabatic exponent and the errors in the experimental quartz Hugoniot, and random uncertainties stemming from measurement errors in the CH and quartz shock velocity. The inferred principal Hugoniot results are consistent with the single-shock data, also showing a change in compressibility around 4 Mbar. It is important to note that the systematic effects involved in each of these data sets are different, making their agreement significant. In the impedance-matching technique, systematic uncertainties arise from uncertainties in quartz's experimental principal Hugoniot and its release behavior, whereas in the inversion method, systematic effects enter through the experimental quartz Hugoniot and the model-based prediction of the CH re-shock density.

The accuracy of the inversion method was tested by using the model-based-averaged adiabatic exponent and the measurable quantities U_{sCH} and U_{sQ} , as predicted by each model. The CH shock velocities used in the analysis spanned a range equivalent to those measured experimentally in the double-shock experiments. The inferred single-shock pressure and density were compared to the pressure and density on the principal Hugoniot, as predicted by each model. Inferred single-shock states were shown to be consistent for all models. For a given pressure, percent differences between density predicted

by models and inferred single-shock density fell between 1%–3%, 1%–2%, and 0.2%–0.3% for *SESAME* 7590, 7591, and 7592, respectively, where differences in density decreased as a function of increasing pressure. This gives confidence that the inversion method leads to accurate results for inferred single-shock conditions.

Quartz is thought to transition from a conducting liquid to a dense plasma at around 4 Mbar. Pressures from 2 to 4 Mbar in

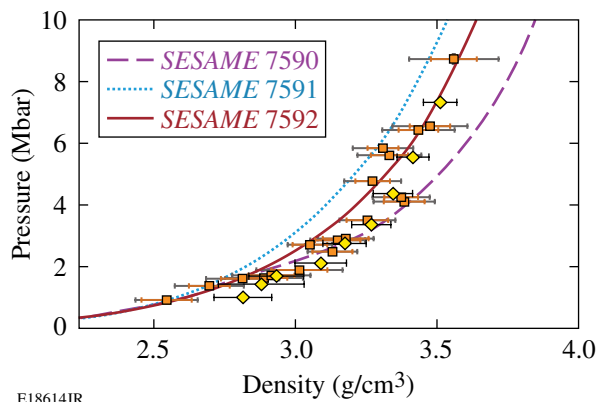


Figure 121.9 Single-shock Hugoniot data for polystyrene as inferred from re-shock (double-shock) data via the inversion method described by Hicks *et al.*³ are shown as yellow diamonds. Uncertainties are shown as black error bars, which represent the total error (quadrature sum of random and systematic uncertainties). Single-shock IM measurements are also shown (orange squares) along with *SESAME* models.³⁸ Inferred single-shock data are consistent with single-shock measurements, where both data sets show stiffening of the material starting at 4 Mbar.

CH correspond to pressure from 3.5 to 7 Mbar in quartz. There was concern that the softening in CH was not its true behavior but rather a manifestation of quartz’s rheology. The fact that the double-shock measurements and the inferred single-shock states display similar behavior to that observed in the single-shock data indicates that the softening is not due to a systematic problem with the quartz release. Moreover, results for CH₂ (see **Polypropylene** below), which encounter similar quartz pressures, show no softening. Again, this indicates that the softening observed in CH is its intrinsic high-pressure behavior.

2. Polypropylene (CH₂)

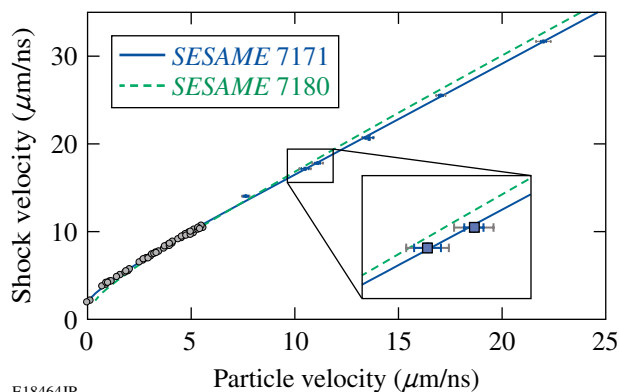
Principal Hugoniot measurements for polypropylene (see Table 121.III) were obtained from 1 to 6 Mbar—the highest published pressure results for this material studied to date. These data have a linear U_s-U_p relation, shown in Fig. 121.10, described by $U_s = (20.025 \pm 0.102) + (1.228 \pm 0.025)(U_p - 12.715)$. A least-squares fitting of the data over an orthogonal polynomial basis was used (using total error) such that the associated errors in the fitting coefficients were uncorrelated. The total uncertainty in the density was between 2.9% and 4.4%. Unlike CH, CH₂ followed a smooth concave trend in the $P-\rho$ plane, with no pressure-induced softening, as shown in Fig. 121.11. On this plane CH₂ was observed to reach lower density for a given pressure, compared to CH. Compression of both CH and CH₂ (see Fig. 121.12) behaved in a similar manner with increasing pressure; therefore, differences in the $P-\rho$ plane were mostly due to density variations in their initial states. *SESAME* 7171 and *SESAME* 7180 are models for branched (polymer has other chains or branches stemming from the main chain backbone) and linear (polymer has atoms arranged in a chain-like struc-

Table 121.III: Polypropylene principal Hugoniot results from impedance matching with quartz reference. Measured shock velocity in the quartz and polypropylene, U_{sQ} and U_{sCH_2} is given with associated random error arising from measurement limitations. U_{pCH_2} (ran,sys), P_{CH_2} (ran,sys), and ρ_{CH_2} (ran,sys) are the resulting particle velocity, pressure, and density of shocked polypropylene obtained through the IM construct. Random errors enter the analysis through measurement uncertainties in U_{sQ} and U_{sCH_2} , while systematic errors emerge from uncertainties in the principal Hugoniot and release states of quartz.

Shot No.	U_{sQ} ($\mu\text{m/ns}$)	U_{sCH_2} ($\mu\text{m/ns}$)	U_{pCH_2} (ran,sys) ($\mu\text{m/ns}$)	P_{CH_2} (ran,sys) (Mbar)	ρ_{CH_2} (ran,sys) (g/cc)
52798	12.14±0.14	14.07±0.11	7.64 (0.12, 0.14)	0.97 (0.02, 0.02)	1.97 (0.04, 0.04)
52797	14.89±0.14	17.2±0.13	10.5 (0.18, 0.22)	1.63 (0.03, 0.03)	2.31 (0.07, 0.08)
52628	15.42±0.1	17.83±0.12	11.11 (0.13, 0.23)	1.78 (0.02, 0.04)	2.38 (0.05, 0.08)
52796	17.65±0.13	20.72±0.1	13.44 (0.16, 0.12)	2.51 (0.03, 0.02)	2.56 (0.06, 0.04)
52631	17.78±0.16	20.74±0.25	13.59 (0.19, 0.12)	2.54 (0.04, 0.02)	2.61 (0.1, 0.05)
52634	21.38±0.1	25.55±0.11	17.05 (0.11, 0.2)	3.92 (0.03, 0.04)	2.71 (0.05, 0.06)
52633	26.42±0.11	31.69±0.12	22 (0.13, 0.33)	6.28 (0.04, 0.09)	2.94 (0.05, 0.1)

ture with no branches) polyethylene (same C-to-H ratio as polypropylene); these models were evaluated at polypropylene's initial density and compared with results.

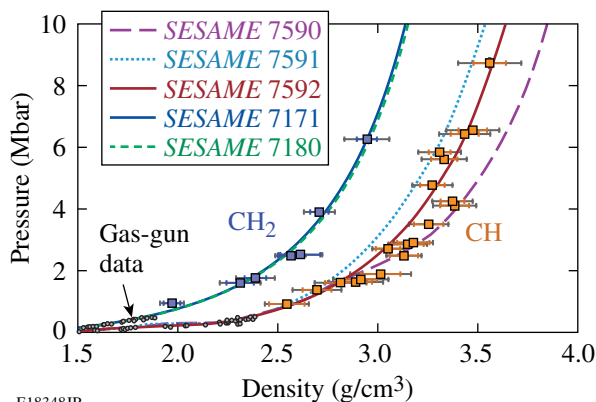
As shown in Figs. 121.10 and 121.11, the CH₂ data are in good agreement with both *SESAME* 7171 and *SESAME* 7180, which predict almost identical behavior in the P - ρ plane. This



E18464JR

Figure 121.10

Principal Hugoniot data and models for CH₂ in the U_s - U_p plane. Data for this study were taken on biaxially oriented polypropylene (C_3H_6)_n with initial density $\rho_0 = 0.9$ g/cc, using IM with quartz reference. Random uncertainties are shown as blue error bars and total uncertainties (quadrature sum of random and systematic errors) are shown as gray error bars. Previous gas-gun experiments from Marsh³⁰ are shown. Data are compared with *SESAME*³⁸ models for polyethylene (C_2H_4)_n evaluated with initial density $\rho_0 = 0.9$ g/cc.

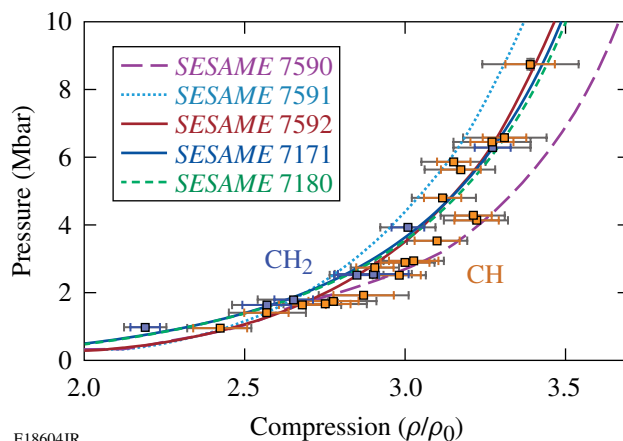


E18348JR

Figure 121.11

Principal Hugoniot data and models for CH₂ and CH in the P - ρ plane (CH models and error bars as in previous figures). Data for CH₂ were taken on biaxially oriented polypropylene (C_3H_6)_n, with initial density $\rho_0 = 0.9$ g/cc, using IM with quartz reference. Random uncertainties are shown as blue error bars and total uncertainties (quadrature sum of random and systematic errors) are shown as gray error bars. Previous gas-gun experiments from Marsh³⁰ are shown. Data for CH₂ are compared with *SESAME*³⁸ models for polyethylene (C_2H_4)_n, evaluated with initial density $\rho_0 = 0.9$ g/cc.

is not entirely surprising since both models make similar physical assumptions with only slightly varying inputs. The electronic contribution was modeled the same way as the *SESAME* models for CH TFD with an exchange constant equal to 2/3. The ground electronic contribution (cold curve) was calculated from shock data and an assumption of a Mie-Grüneisen EOS, where the reference Grüneisen parameter was calculated in the same manner as in the CH *SESAME* models, leading to values 0.561 and 0.739 for *SESAME* 7171 and 7180, respectively. The reference Debye temperature was calculated from the U_s - U_p intercept, average atomic weight, initial density, and a Poisson ratio of 1/3. The nuclear contribution was obtained via a solid-gas interpolation formula, which is in agreement with the Debye formula at low temperatures or high densities and approaches the ideal gas at high temperatures or low densities. Differences in the models arise from experimental Hugoniot data used to construct the cold curve and parameters derived from other experimental measurements, such as the reference Grüneisen coefficient and Debye temperature, used to compute the lattice vibrational contribution. The cohesive energies were set at 3.35 and 4 MJ/kg for *SESAME* 7171 and 7180, and binding energies resulting from cold-curve calculations differed by ~3%. The atomic number and atomic weight were assumed to be 8/3 and 4.6757, respectively.^{47,48}



E18604JR

Figure 121.12

Principal Hugoniot measurements for CH and CH₂ in the P - η plane using quartz as IM reference. Models and error bars as described in previous figures.

Optical and Thermal Measurements

1. Reflectivity

The reflectivity of the observed shocks was determined by the signal level of the probe beam detected by the VISAR streak camera. The incident probe intensity was essentially constant over its pulse duration. That intensity was normalized using the detected levels produced by the α -quartz pusher, whose

reflectivity as a function of shock velocity is known.¹⁸ This leads to continuous records of reflectivity as a function of time for materials under study. However, the intensity profiles in CH showed an anomalous behavior: the detected intensity increased as the decaying shock transited the sample. This behavior was amplified with increasing pressure. This was the result of a “fogging” in the CH that attenuated the VISAR probe beam. X rays from the laser plasma were absorbed in the sample material, producing free electrons that can absorb light, although insufficient to produce noticeable preheat.⁴⁹ As the shock front (which was decaying in strength) moved through the CH, the VISAR probe beam passed through less-absorbing material, causing the streak cameras to register an increase in intensity signal levels, even though the shock was decaying. The anomalous behavior was observed in CH but not observed in CH₂ at low pressures, where the intensity decreased as a function of time, as expected. Anomalous behavior of CH₂ was observed only at the highest-pressure experiment. To account for this, reflectivity data were calculated only at the quartz–CH (CH₂) interface. Here the quartz signal was attenuated by the same amount as the CH signal, and the normalization to the known quartz reflectivity held. To do this, the intensity returned from the shocked pusher (quartz) and polymer was linearly fit and extrapolated to the contact interface. The reflected intensities and the known reflectivity of quartz (as a function of shock velocity) provided reflectance measurements for the hydrocarbons. For CH, this led to one data point $R(U_s)$, translated to $R(P)$, having knowledge of the pressure obtained from a corresponding CH shock/velocity value via IM. Continuous $R(U_s)$ measurements were obtained for CH₂ at low pressures, but for precaution, only reflectivities at the contact interface were used, resulting in one $R(P)$ data point; this also translates to temperature measurements since they are dependent on measured reflectance. The reflectivity of CH and CH₂ as a function of pressure is shown in Fig. 121.13. Errors in reflectivity varied from 31% at the lowest pressure to 9% at the highest pressure for CH and from 25% to 15% from lowest to highest pressure for CH₂. At higher pressures, there was a better signal-to-noise ratio since the shocked hydrocarbons became better reflectors. Low-pressure measurements in the hydrocarbons corresponded to pressures of 1 to 2 Mbar in quartz, close to its melt onset. At these pressures, quartz is barely reflective and the reflected intensity measurements are less accurate.

Both CH and CH₂ underwent a drastic increase in reflectivity at around 1 Mbar and saturated at ~40%. This occurred at 2.5 to 3 Mbar for both materials. This behavior—steep reflectivity increase and saturation—is often seen in materials undergoing an insulator–conductor transition.^{50–52}

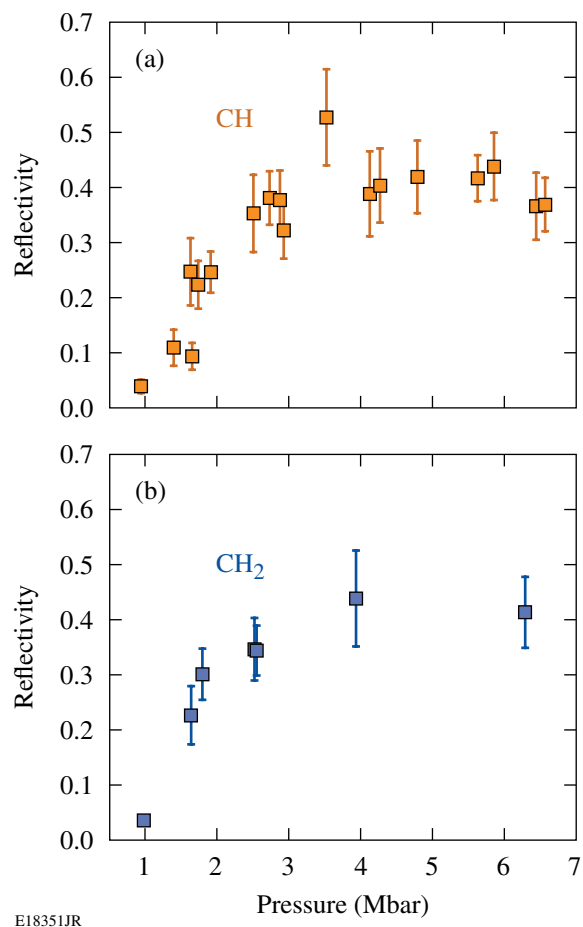


Figure 121.13 Reflectivity measurements from VISAR signal and quartz known reflectivity for (a) polystyrene and (b) polypropylene, where saturation occurs at 40% for both materials.

Polystyrene’s optical properties have been previously studied by Koenig *et al.*⁵³ with CH shock velocities of 11 to 16 $\mu\text{m/ns}$ (~0.8 to 1.7 Mbar), where they observed steadily increasing reflectivities reaching values up to 50%, well above our measurements. In that same pressure range, we observed smaller reflectivities, <25%. The reflectivity of shocked CH was also measured by Ozaki *et al.*¹⁰ who found reflectivities from 16% to 42% in the CH shock-velocity range of ~22 to 27 $\mu\text{m/ns}$ (~3 to 5 Mbar), in better agreement with our findings.

Discrepancies in reflectivities between studies could arise from differences in diagnostic configurations or from probe-beam stability. Reflectivity measurements in these studies are relative measurements since reflected intensities between a standard material and sample are compared and “normalized” with known reflectivities of the unshocked or shocked standard. If the probe-beam stability is compromised either temporally

or spatially and the analysis does not correct for it, this could yield biased reference reflectivities. In these experiments a reference image of the returned probe intensity is acquired on each shot. These were used to monitor deviations in the incident probe-beam intensity, which were quite small.

2. Temperature

The brightness temperatures of the shocks were determined from spectral radiance intensities detected by the SOP with a wavelength range of 590 to 900 nm, with a centroid wavelength of 682 nm (Ref. 28). Recorded SOP intensities were modeled assuming a gray-body Planckian spectrum given by

$$L(\lambda, T) = \varepsilon(\lambda) \frac{2hc^2}{\lambda^5} \frac{1}{e^{hc/\lambda T} - 1},$$

where ε is the emissivity, h is Planck's constant, c is the speed of light, λ is the radiation wavelength, and T is the temperature of a Planckian radiator.

The emissivity is given by $1-R(\lambda)$, where $R(\lambda)$ is the reflectivity that is assumed to vary only slightly as a function of wavelength in the optical spectral range, such that $R(\lambda)$ is the same optical reflectivity measured by VISAR at 532 nm. As described in **Reflectivity** (p. 16), reflectivity values were obtained by linearly fitting the VISAR intensities and extrapolating to the contact interface, avoiding attenuation effects of the VISAR probe beam in polystyrene. Consequently the recorded SOP spectral intensities emitted by the shocked polymer were linearly fit over a time interval of ~ 500 to 600 ps and extrapolated to a time corresponding to that of the contact interface, such that obtained reflectivity measurements could be used for emissivity calculations. This implies that SOP measurements were taken close to the quartz–glue–CH boundary. SOP has a temporal resolution of ~ 170 ps; therefore, the self-emission from the shock front is integrated over this time interval. At material boundaries, the recorded SOP intensity could be the integrated signal from different materials. Large time intervals were chosen to linearly fit the SOP data with this in mind. Material boundaries on SOP records are not easily identified (as on VISAR records); therefore, care was taken to choose/define the beginning of a material region, containing a signal for such material, only after the SOP signal had recovered from observable spectral-intensity changes.

Having observed absorption of the VISAR probe beam in CH (at all pressures) and CH₂ (at the highest pressure only), there was concern that spectral intensities as recorded by SOP

were affected as well. To account for this, the sample temperatures were normalized to the quartz. Quartz reflectivity and temperature as functions of pressure (shock velocity) have been previously studied.¹⁶ Since the quartz and polymer signal in the SOP diagnostic are subject to the same conditions (optical path, camera sensitivity, and resulting spectral response of the diagnostic), one can re-derive the equation for the temperatures in the sample by substituting diagnostic constants with the quartz's observed temperature and emissivity. The resulting sample temperatures are relative temperatures since they are referenced, or normalized, to the quartz's known shock Hugoniot thermal and optical behavior.

Tables 121.IV and 121.V list the brightness and normalized temperatures for CH and CH₂, respectively. The brightness temperatures are those derived simply from the measured spectral intensity and the SOP calibration. The normalized temperatures use the observed brightness of the quartz shock plus its velocity to provide a normalization that is applied to the CH and CH₂ results. On average, normalized temperatures for CH were $\sim 1.3\times$ larger than those measured using CH SOP intensities only; for CH₂ that factor was ~ 1.1 . [It should be noted that two shots (52628 and 52631), each simultaneously studying both CH and CH₂, showed brightness temperatures that were higher than shots at similar conditions. When normalized to quartz, those temperatures had negligible changes. This suggests that for some reason these two shots did not experience fogging in the samples.]

Table 121.IV: Hugoniot temperatures for polystyrene as obtained using reflectivity and SOP spectral intensities for each shot. Relative temperatures, normalized to quartz, show that polystyrene's behavior also affects SOP spectral intensities.

Shot No.	T (eV)	$T_{\text{normalized}}$ (eV)
52795	0.43±0.05	0.51±0.05
52800	0.59±0.03	1.06±0.07
52793	0.70±0.06	0.88±0.10
52464	0.63±0.07	1.01±0.13
52628	1.22±0.06	1.19±0.06
52792	1.05±0.08	1.39±0.17
52631	1.97±0.21	1.95±0.18
52799	1.38±0.09	1.79±0.17
52791	1.75±0.32	2.50±0.57
52634	2.25±0.35	2.84±0.43
52633	4.29±0.52	5.57±0.62

Table 121.V: Hugoniot temperatures for polypropylene as obtained using the reflectivity and SOP spectral intensities for each shot. Relative temperatures, normalized to quartz, were also obtained.

Shot No.	T (eV)	$T_{\text{normalized}}$ (eV)
52798	0.46 ± 0.06	0.53 ± 0.05
52797	0.70 ± 0.05	0.81 ± 0.08
52628	1.02 ± 0.06	1.05 ± 0.08
52796	0.95 ± 0.06	1.15 ± 0.11
52631	1.44 ± 0.09	1.42 ± 0.13
52634	2.18 ± 0.40	2.42 ± 0.43
52633	3.86 ± 0.59	5.01 ± 0.81

Figure 121.14 shows normalized temperatures for polystyrene [orange points in (a)] and polypropylene [blue points in (b)]. Temperature errors were between 5% and 22% for CH and 8% and 18% for CH₂; these errors stemmed from system calibration and measurements of self-emission and reflectivity in each hydrocarbon. Quartz parameters for normalization were taken from a fit to the data in Ref. 16. The various *SESAME* models available for CH and CH₂ predict similar thermal behavior for both materials: both materials reach comparable temperatures from ~1 to 7 Mbar. The models predict similar shock temperatures that all agree fairly well with measurements over that range. The models are similar enough to each other that the data, with their moderate precision, do not favor any one of the models. CH temperatures at 3 to 5 Mbar by Ozaki *et al.*¹⁰ [green points in Fig. 121.14(a)] are consistent with these data.

Conclusions

The equation of state was measured for two hydrocarbons at shock pressures of 1 to 10 Mbar. A time-resolved VISAR diagnostic provided precise (~1%) measurement of shock velocity in the transparent standard and sample materials. The use of experimental data for the Hugoniot of the quartz pusher made it possible to determine the systematic errors in the IM technique for the derived quantities. These data are the most-precise measurements of the EOS of hydrocarbons performed at these high pressures (≥ 1 Mbar).

Polystyrene (CH) was observed to compress by 2.5 \times to ~3.5 \times at pressures of 1 to 10 Mbar. This behavior was predicted by the *SESAME* 7592 model. Polystyrene exhibits slightly greater compressibility (compared to *SESAME* 7592) in the 2- to 4-Mbar range. Previous results from other researchers showed much stiffer behavior, most likely due to preheating of those samples.

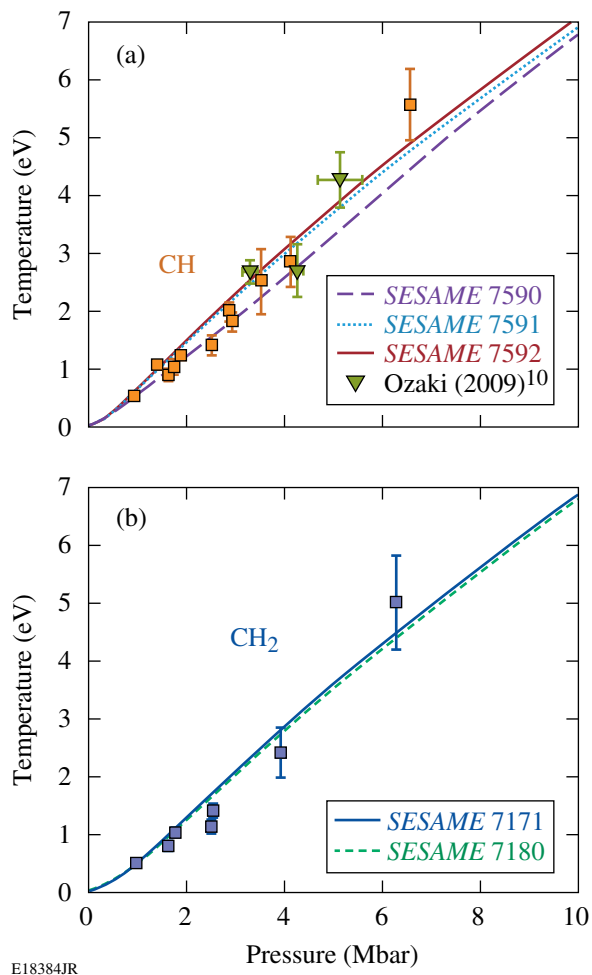


Figure 121.14

Temperature measurements were calculated from SOP self-emission records, fitted to a gray-body Planckian radiator, where emissivity was obtained from reflectivity measurements from VISAR, and normalized using the known quartz temperature and reflectivity. Both (a) polystyrene and (b) polypropylene reach similar temperatures with increasing pressure.

Polypropylene (CH₂) was observed to compress by similar amounts over a similar range of pressures. Two *SESAME* models (7171 and 7180) reproduced the behavior well (in this pressure range, the two models for polypropylene were nearly indistinguishable). This agreement for both materials suggests that the effect of the C-to-H ratio is properly accounted for in these models for polystyrene and polypropylene.

Reflectivity measurements indicated that both polystyrene and polypropylene become reflective when shocked to 1 to 2 Mbar. Above 3 Mbar, shock waves in both materials have a reflectivity of ~40%. This behavior is typical of materials that undergo a shock-induced transition from an insulator to a conductor.

The measured intensity of the self-emission from these shocks, normalized to known temperatures in quartz, was used to infer the brightness temperature of shocks in the two materials. Reflectivity measurements were used to infer gray-body brightness temperatures of the shock waves. The results show that both polystyrene and polypropylene are heated to 0.5 to 5 eV by shock pressures of ~ 1 to 6 Mbar. The shock temperatures in each material are well predicted by the *SESAME* models, but the models are so similar that no model is favored. Normalized temperatures showed consistent differences from brightness temperatures, and it was concluded that partial blanking of the SOP diagnostic occurred. This was evident in the CH at all pressures and only at the highest pressure for CH₂.

These results are significant in that they provide high-precision kinematic and thermal data for two hydrocarbons shocked to 1 to 10 Mbar, providing a complete EOS of those materials. The polystyrene data indicate that this material does not stiffen at high pressures (as suggested by earlier experiments), and the polypropylene data show that the effect of the C-to-H ratio is reasonably predicted by the models. These results are particularly important to the design of ICF targets for the NIF, which will use similar hydrocarbon ablaters that are compressed by multiple shocks in this pressure region. Similarly, the behavior of hydrocarbons shocked to ~ 10 Mbar is important to general studies of high-energy-density physics.

ACKNOWLEDGMENT

This work was supported by the U.S. Department of Energy Office of Inertial Confinement Fusion under Cooperative Agreement No. DE-FC52-08NA28302, the University of Rochester, and the New York State Energy Research and Development Authority. The support of DOE does not constitute an endorsement by DOE of the views expressed in this article.

REFERENCES

1. D. G. Hicks, T. R. Boehly, P. M. Celliers, J. H. Eggert, E. Vianello, D. D. Meyerhofer, and G. W. Collins, *Phys. Plasmas* **12**, 082702 (2005).
2. D. G. Hicks, T. R. Boehly, P. M. Celliers, D. K. Bradley, J. H. Eggert, R. S. McWilliams, R. Jeanloz, and G. W. Collins, *Phys. Rev. B* **78**, 174102 (2008).
3. D. G. Hicks, T. R. Boehly, P. M. Celliers, J. H. Eggert, S. J. Moon, D. D. Meyerhofer, and G. W. Collins, *Phys. Rev. B* **79**, 014112 (2009).
4. J. D. Lindl *et al.*, *Phys. Plasmas* **11**, 339 (2004).
5. S. W. Haan *et al.*, *Phys. Plasmas* **2**, 2480 (1995).
6. S. W. Haan *et al.*, *Phys. Plasmas* **12**, 056316 (2005).
7. S. W. Haan *et al.*, *Eur. Phys. J. D* **44**, 249 (2007).
8. R. Cauble *et al.*, *Phys. Plasmas* **4**, 1857 (1997).
9. N. Ozaki *et al.*, *Phys. Plasmas* **12**, 124503 (2005).
10. N. Ozaki *et al.*, *Phys. Plasmas* **16**, 062702 (2009).
11. T. R. Boehly, D. H. Munro, P. M. Celliers, R. E. Olson, D. G. Hicks, V. N. Goncharov, G. W. Collins, H. F. Robey, S. X. Hu, J. A. Marozas, T. C. Sangster, O. L. Landen, and D. D. Meyerhofer, *Phys. Plasmas* **16**, 056302 (2009).
12. G. R. Moore and D. E. Kline, *Properties and Processing of Polymers for Engineers* (Prentice-Hall, Englewood Cliffs, NJ, 1984).
13. F. H. Ree, *J. Chem. Phys.* **70**, 974 (1979).
14. W. J. Nellis *et al.*, *J. Chem. Phys.* **80**, 2789 (1984).
15. W. J. Nellis, D. C. Hamilton, and A. C. Mitchell, *J. Chem. Phys.* **115**, 1015 (2001).
16. D. G. Hicks, T. R. Boehly, J. H. Eggert, J. E. Miller, P. M. Celliers, and G. W. Collins, *Phys. Rev. Lett.* **97**, 025502 (2006).
17. T. R. Boehly, J. E. Miller, D. D. Meyerhofer, J. G. Eggert, P. M. Celliers, D. G. Hicks, and G. W. Collins, in *Shock Compression of Conducted Matter—2007*, edited by M. Elert *et al.* (American Institute of Physics, Melville, NY, 2007), Vol. 955, pp. 19–22.
18. S. Brygoo, D. G. Hicks, P. Loubeyre, J. H. Eggert, S. McWilliams, P. M. Celliers, T. R. Boehly, R. Jeanloz, and G. W. Collins, “Development of Melted Quartz as an Impedance-Matching Standard for Strong Laser Shock Measurements,” to be published in the *Journal of Applied Physics*.
19. T. R. Boehly, R. S. Craxton, T. H. Hinterman, J. H. Kelly, T. J. Kessler, S. A. Kumpan, S. A. Letzring, R. L. McCrory, S. F. B. Morse, W. Seka, S. Skupsky, J. M. Soures, and C. P. Verdon, *Rev. Sci. Instrum.* **66**, 508 (1995).
20. Y. Lin, T. J. Kessler, and G. N. Lawrence, *Opt. Lett.* **20**, 764 (1995).
21. Ya. B. Zel’dovich and Yu. P. Raizer, in *Physics of Shock Waves and High-Temperature Hydrodynamic Phenomena*, edited by W. D. Hayes and R. F. Probstein (Dover Publications, Mineola, NY, 2002), Vol. I, Chap. I, pp. 1–104.
22. R. P. Drake, *High-Energy-Density Physics: Fundamentals, Inertial Fusion, and Experimental Astrophysics*, Shock Wave and High Pressure Phenomena (Springer, Berlin, 2006).
23. P. M. Celliers, D. K. Bradley, G. W. Collins, D. G. Hicks, T. R. Boehly, and W. J. Armstrong, *Rev. Sci. Instrum.* **75**, 4916 (2004).
24. P. M. Celliers *et al.*, *Appl. Phys. Lett.* **73**, 1320 (1998).
25. L. M. Barker and R. E. Hollenbach, *J. Appl. Phys.* **43**, 4669 (1972).
26. L. M. Barker and K. W. Schuler, *J. Appl. Phys.* **45**, 3692 (1974).

27. P. A. Jaanimagi, R. Boni, D. Butler, S. Ghosh, W. R. Donaldson, and R. L. Keck, in *26th International Congress on High-Speed Photography and Photonics*, edited by D. L. Paisley *et al.* (SPIE, Bellingham, WA, 2005), Vol. 5580, pp. 408–415.
28. J. E. Miller, T. R. Boehly, A. Melchior, D. D. Meyerhofer, P. M. Celliers, J. H. Eggert, D. G. Hicks, C. M. Sorce, J. A. Oertel, and P. M. Emmel, *Rev. Sci. Instrum.* **78**, 034903 (2007).
29. G. A. Lyzenga, T. J. Ahrens, and A. C. Mitchell, *J. Geophys. Res. B* **88**, 2431 (1983).
30. S. P. Marsh, ed. *LASL Shock Hugoniot Data*, Los Alamos Series on Dynamic Material Properties (University of California Press, Berkeley, CA, 1980).
31. R. F. Trunin *et al.*, *Izv. Acad. Sci. USSR Phys. Solid Earth*, **8** (1971).
32. R. F. Trunin, *Phys.-Usp.* **37**, 1123 (1994).
33. Recent work on the Sandia Z Machine by Knudson, first presented at 16th Topical Conference on Shock Compression of Condensed Matter, measured Hugoniot and sound speed of α -quartz in the 1- to 16-Mbar regime, observing some curvature in $U_s(U_p)$. [M. Knudson and M. Desjarlais, presented at the 16th APS Topical Conference on Shock Compression of Condensed Matter, Nashville, TN, 28 June–3 July 2009 (Paper V2.00001); M. Knudson, *Bull. Am. Phys. Soc.* **54**, 134 (2009).] If real, this can cause shifts in the data obtained using α -quartz as an IM standard, although it does not compromise the precision of the data presented in this article. To resolve this, measurement of the Mie–Grüneisen parameter using laser-driven shock waves is currently underway. The data presented here will be reanalyzed with this new data in a future publication. The percent difference in density between the fit found by Knudson and that used in this study varies with quartz shock velocity, peaking around 19 to 20 km/s (6 to 7 Mbar) at ~6% and decreasing with increasing shock velocity and pressure. This implies that values would be most compromised only in these ranges, and data obtained at higher pressures would be less affected.
34. R. G. McQueen, Los Alamos National Laboratory, Los Alamos, NM, LA-UR-90-1996 (1989).
35. R. F. Trunin, *Shock Compression of Condensed Materials* (Cambridge University Press, Cambridge, England, 1998).
36. A. N. Mostovych *et al.*, *Phys. Plasmas* **8**, 2281 (2001).
37. T. R. Boehly, D. G. Hicks, P. M. Celliers, T. J. B. Collins, R. Earley, J. H. Eggert, D. Jacobs-Perkins, S. J. Moon, E. Vianello, D. D. Meyerhofer, and G. W. Collins, *Phys. Plasmas* **11**, L49 (2004).
38. S. P. Lyon and J. D. Johnson, Los Alamos National Laboratory, Los Alamos, NM, Report LA-CP-98-100 (1998).
39. N. C. Holmes, *Rev. Sci. Instrum.* **62**, 1990 (1991).
40. I. P. Dudoladov *et al.*, *Prikl. Mekh. Tekh. Fiz.* **4**, 148 (1969).
41. R. G. McQueen *et al.*, in *High-Velocity Impact Phenomena*, edited by R. Kinslow (Academic Press, New York, 1970), Chap. VII, Sec. II, pp. 293–417.
42. M. Van Thiel, J. Shaner, and E. Salinas, Lawrence Livermore National Laboratory, Livermore, CA, Report UCRL-50108, Rev. 1 (1977).
43. A. V. Bushman *et al.*, *JETP Lett.* **82**, 895 (1996).
44. J. Abdallah, Jr., Los Alamos National Laboratory, Los Alamos, NM, Report LA-10244-M, NTIS Order No. DE85001405 (1984). (Copies may be obtained from the National Technical Information Service, Springfield, VA 22161.)
45. G. I. Kerley, Sandia National Laboratory, Albuquerque, NM, Report SAND-88-2291, NTIS Order No. DE91017717 (1991). (Copies may be obtained from the National Technical Information Service, Springfield, VA 22161.)
46. R. Cauble (Lawrence Livermore National Laboratory) and N. Ozaki (Osaka University), private communication (2009).
47. F. Dowell, Los Alamos National Laboratory, Los Alamos, NM, Report LA-9559-MS, NTIS Order No. DE83003896 (1982). (Copies may be obtained from the National Technical Information Service, Springfield, VA 22161.)
48. F. Dowell, Los Alamos National Laboratory, Los Alamos, NM, Report LA-9564-MS, NTIS Order No. DE83004996 (1982). (Copies may be obtained from the National Technical Information Service, Springfield, VA 22161.)
49. W. Theobald, J. E. Miller, T. R. Boehly, E. Vianello, D. D. Meyerhofer, T. C. Sangster, J. Eggert, and P. M. Celliers, *Phys. Plasmas* **13**, 122702 (2006).
50. D. K. Bradley *et al.*, *Phys. Rev. Lett.* **93**, 195506 (2004).
51. P. M. Celliers *et al.*, *Phys. Rev. Lett.* **84**, 5564 (2000).
52. P. M. Celliers *et al.*, *Phys. Plasmas* **11**, L41 (2004).
53. M. Koenig *et al.*, *Phys. Plasmas* **10**, 3026 (2003).